

# PROCEEDINGS OF SPIE

[SPIDigitalLibrary.org/conference-proceedings-of-spie](https://SPIDigitalLibrary.org/conference-proceedings-of-spie)

## In-line Raman spectroscopy for stacked nanosheet device manufacturing

Schmidt, D., Durfee, C., Li, J., Loubet, N., Cepler, A., et al.

D. Schmidt, C. Durfee, J. Li, N. Loubet, A. Cepler, L. Neeman, N. Meir, J. Ofek, Y. Oren, D. Fishman, "In-line Raman spectroscopy for stacked nanosheet device manufacturing," Proc. SPIE 11611, Metrology, Inspection, and Process Control for Semiconductor Manufacturing XXXV, 116111T (25 February 2021); doi: 10.1117/12.2582181

**SPIE.**

Event: SPIE Advanced Lithography, 2021, Online Only

# In-Line Raman Spectroscopy for Stacked Nanosheet Device Manufacturing

D. Schmidt<sup>a,\*</sup>, C. Durfee<sup>a</sup>, J. Li<sup>a</sup>, N. Loubet<sup>a</sup>, A. Cepler<sup>b</sup>, L. Neeman<sup>c</sup>, N. Meir<sup>c</sup>,  
J. Ofek<sup>c</sup>, Y. Oren<sup>c</sup>, D. Fishman<sup>c</sup>

<sup>a</sup>IBM Research, 257 Fuller Road, Albany, NY, USA 12203

<sup>b</sup>Nova Measuring Instruments Inc, 3342 Gateway Blvd, Fremont, CA, USA 93117

<sup>c</sup>Nova Measuring Instruments Ltd, 5 David Fikes St, Rehovot, Israel 7610201

\*schmidt@ibm.com

## ABSTRACT

In-line Raman spectroscopy for compositional and strain metrology throughout front-end-of-line manufacturing of next-generation stacked gate-all-around nanosheet field-effect transistors is presented. Thin and alternating layers of fully strained pseudomorphic  $\text{Si}_{(1-x)}\text{Ge}_x$  and Si were grown epitaxially on a Si substrate and subsequently patterned. Intentional strain variations were introduced by changing the Ge content ( $x = 0.25, 0.35, 0.50$ ). Polarization-dependent in-line Raman spectroscopy was employed to characterize and quantify the strain evolution of Si and  $\text{Si}_{(1-x)}\text{Ge}_x$  nanosheets throughout front-end-of-line processing by focusing on the analysis of Si-Si and Si-Ge optical phonon modes. To evaluate the accuracy of the Raman metrology results, strain reference data were acquired by non-destructive high-resolution x-ray diffraction and from destructive lattice deformation maps using precession electron diffraction. It was found that the germanium-alloy composition as well as Si and  $\text{Si}_{(1-x)}\text{Ge}_x$  strain obtained by Raman spectroscopy are in excellent agreement with reference metrology and follow trends of previously published simulations.

**Keywords:** Raman spectroscopy, strain, stress, gate-all-around, nanosheet FET

## 1. INTRODUCTION

Stacked nanosheet gate-all-around (GAA) field effect transistors (FETs) will be the next-generation device architecture replacing finFET technology either next year or in 2023.<sup>1</sup> The new transistor type is an evolutionary step from finFETs with better performance due to superior electrostatics and short channel control, for example.<sup>2</sup> A nanosheet GAAFET may be viewed, in a simplistic manner, as a finFET rotated on its side, where the fin is now a horizontal nanosheet with a gate wrapped around the entire perimeter. Typically, the device comprises three or more vertically stacked individual horizontal nanosheets, which serve as channels. This is accomplished by first growing alternating pseudomorphic  $\text{Si}_{(1-x)}\text{Ge}_x$  and Si layers on a Si substrate. Here, a perfect crystal quality is critical to achieve defect free, biaxially strained  $\text{Si}_{(1-x)}\text{Ge}_x$  and strain free Si single crystalline layers. This multilayer stack is then patterned in both in-plane orientations to define channel length and width. Usually, the  $\text{Si}_{(1-x)}\text{Ge}_x$  sheets are sacrificial and removed soon after source/drain epitaxy leaving the Si sheets as transport channels.<sup>2</sup> In order to pursue optimum transistor performance, it is desirable to increase charge carrier mobility through tensile and compressive strain for nFET and pFET, respectively. The electron mobility in GAA nFET Si channels is intrinsically higher than that of finFETs due to the sheet orientation and some residual tensile strain after patterning. However, the advantages for nFET negatively impact the pFET hole mobility. Additionally, as the transistor volume shrinks due to aggressive pitch scaling and three-dimensional stacking, traditional external channels stressors are often not very effective. Besides that, integration schemes of horizontal nanosheets wrapped with high-k/metal gate materials create many unconstrained free surfaces throughout the patterning process, leading to natural relaxation. Overcoming these challenges requires either complex and costly manufacturing schemes or innovative strain engineering approaches.<sup>3,4</sup>

No matter which integration scheme is pursued, the complex manufacturing process, particularly related to the channels and their immediate environment, requires tight specification limits and hence additional, more advanced, and novel in-line metrology capabilities compared to previous transistor architectures. Specifically, monitoring and controlling strain at such small scales and within intricate nanoscale device structures is a new challenge and a suitable non-destructive and

fast in-line technique is critical for successful research and development as well as manufacturing. Relying on destructive imaging and in-line electrical test results is not a viable option for competitive development or efficient and economical high-volume manufacturing.

So far, quantitative strain measurements for GAAFETs are relying on scanning transmission electron microscope (STEM) based techniques. The strain is measured by either nanobeam diffraction, geometrical phase analysis or most precisely by precession electron diffraction (PED). Beam diameters of approximately 5 nm allow mapping of channel strain even in aggressively scaled FETs with channel lengths of less than 20 nm.<sup>4-7</sup> However, TEM techniques are time-consuming, destructive, and require sample preparation, which may influence strain characteristics.

Non-destructive high-resolution X-ray diffraction (XRD) techniques usually require a large spot size and long measurement times due to the limited brightness of available fab tools sources. Furthermore, the signal to noise ratio depends on the interaction volume, which makes measurements of patterned samples with thin films and low areal density difficult. With continued scaling and hence smaller pitches, larger reciprocal space maps are required to capture enough information for strain evaluation, which additionally affects the measurement time. Schulze *et al.* reported reciprocal space maps in the vicinity of the asymmetric (113) Bragg reflection parallel and perpendicular to patterned fins. While they concluded that the multilayer fins are fully strained along the fin direction and partially relaxed perpendicular to it, no quantitative results are presented.<sup>8</sup>

In this work, for the first time, in-line Raman spectroscopy is presented for non-destructive strain metrology at seven different process steps throughout the front-end-of-line (FEOL) manufacturing cycle of stacked GAAFETs. The strain evolution is tracked for three experimental scenarios with intentionally different initial strain conditions. Here, focus is put on nFET device baseline monitoring. The determined strain is compared to reference metrology and discussed with respect to recently published simulation results.<sup>5,6</sup>

## 2. EXPERIMENTAL DETAILS

For this study, stacked nanosheet GAA nFETs were manufactured in a very similar manner to what was published earlier.<sup>2</sup> The nanosheet stack is composed of alternating  $\text{Si}_{(1-x)}\text{Ge}_x$  and Si layers, three each, grown on a Si substrate. The only intentional variation introduced in the manufacturing process was during nanosheet stack epitaxy. The experiment comprises three different split conditions where the sacrificial  $\text{Si}_{(1-x)}\text{Ge}_x$  nanosheet layers are pseudomorphically grown with varying Ge content (nominally  $x = 0.25, 0.35, 0.50$ ). This introduces different initial biaxial strain conditions since the compressive strain in defect-free pseudomorphic  $\text{Si}_{(1-x)}\text{Ge}_x$  layers increases monotonically with  $x$  due to the increasing lattice mismatch with Si.

In-line polarized Raman spectroscopy measurements were carried out on a commercially available 300 mm fab tool (Nova ELIPSON) after seven different processing steps throughout the front-end of line manufacturing cycle: (i) post nanosheet stack epitaxy, (ii) post fin patterning, (iii) post dummy gate patterning, (iv) post fin recess (second fin patterning), (v) post source/drain (S/D) epitaxy, (vi) post dummy gate removal, and (vii) post channel release. Multiple targets with varying fin and gate critical dimensions (CDs) were measured for 21 fields across the wafer to evaluate the dimensional dependence of strain as well as the across wafer characteristics. The experimental settings are such that most if not all Si and  $\text{Si}_{(1-x)}\text{Ge}_x$  nanosheets contribute to the Raman scattering response. Hence results must be understood as average characteristics of all probed sheets over an array of multiple fins and gates where present.

After the nanosheet stack epitaxy in-line high-resolution  $\omega$ - $2\theta$ XRD scans (Bruker J VX7300LSI) around the (004) Bragg reflection were analyzed to determine sheet thickness and Ge content. Data was acquired at five different locations across the wafer. Additionally, asymmetric (113) reciprocal space maps were acquired to confirm defect-free pseudomorphic growth of the  $\text{Si}_{(1-x)}\text{Ge}_x$  sheets. Due to the long measurement times, only one RSM was acquired per sample. With the confirmation of defect-free single crystalline films, the in-plane sheet strain can then be calculated based on the Ge content dependent alloy lattice mismatch.<sup>9</sup>

Furthermore, in-plane  $\text{Si}_{(1-x)}\text{Ge}_x$  sheet strain based on destructive lattice deformation maps was calculated post fin patterning. The maps were determined from nano-beam PED patterns acquired with a convergence semi-angle of 2.5 mrad, a beam precession at 200 Hz at an angle of 0.35°, and an exposure time of 50 ms. The unstrained Si reference is taken from the fin base away from the nanosheet stacks.<sup>7</sup>

### 3. RAMAN SPECTROSCOPY

Raman spectroscopy has long been shown to be an excellent non-destructive technique to measure stress in Si-based semiconductor devices.<sup>10-12</sup> It relies on inelastic scattering of incident photons, which interact with vibrational energy states of the sample system. The scattered light can be either lower (Stokes Raman scattering) or higher (anti-Stokes Raman scattering) in energy and the magnitude of the shift corresponds to the specific vibrational modes. The energy shift depends strongly on the exact geometry and length of atomic bonds and hence the Raman scattering response is a unique signature of composition and structure. Therefore, analyzing the Raman fingerprint of a sample allows for determination of characteristics such as composition, strain, and crystallinity, for example.

From an experimental point of view, the choice of excitation energy along with polarization settings within the incident and scattered beam paths are most critical considerations. Depending on the sample under investigation, the incident wavelength determines penetration depth and Raman scattering efficiency. For example, the penetration depth for an excitation wavelength of 400 nm in SiGe<sub>25</sub> is about 30 nm, while 450 nm penetrate already around 200 nm into the film. Hence, shorter wavelengths probe rather in the vicinity of the surface, and with longer wavelengths, information from deeper sample regions can be accessed. The Raman scattering efficiency and therefore the Raman peak intensity strongly depends on the composition of Si<sub>(1-x)</sub>Ge<sub>x</sub>, for instance. Shorter wavelengths are desired for silicon-rich and longer wavelengths for germanium-rich alloys, respectively.<sup>13</sup>

Equally important is polarization control when measuring single crystalline films or anisotropic samples, for instance. Yoo *et al.* have shown the polarization-dependence of Raman signals from bare Si wafers: the intensity as well as the peak position depend on the crystallographic orientation.<sup>14</sup> Particularly important are polarization-dependent Raman measurements when the samples are patterned. Figure 1a illustrates how the Raman scattering intensities as a function of wavenumber depend on the polarization orientation. Here, the sample is a stack of alternating pseudomorphic SiGe<sub>35</sub> and Si layers on a Si substrate post patterning (Figure 1b). A gradual transition of the polarization direction from parallel to perpendicular to the fins reveals successively dramatic changes. The peak intensity around 510 cm<sup>-1</sup> steadily decreases while the position remains constant. The peak around 520 cm<sup>-1</sup> is slightly increasing in intensity and shifting toward higher wavenumbers. Raman selection rules and polarization-specific near-field interactions are responsible for the observed Raman spectra. Finite difference time domain (FDTD) simulations show that when the light polarization is parallel to the fins, the electric field is concentrated within the fin feature and the response dominated by the stacked Si<sub>65</sub>Ge<sub>35</sub> and Si layers (Figure 1c). With light polarization in the orthogonal direction (perpendicular to the fins), the electric field is mostly excluded from the fin and the observed Raman spectrum is dominated rather by the Si substrate (Figure 1d). Since Raman scattering depends on the fourth power of the local electric field, the simulations indicate that polarization-dependent measurements are highly selective.

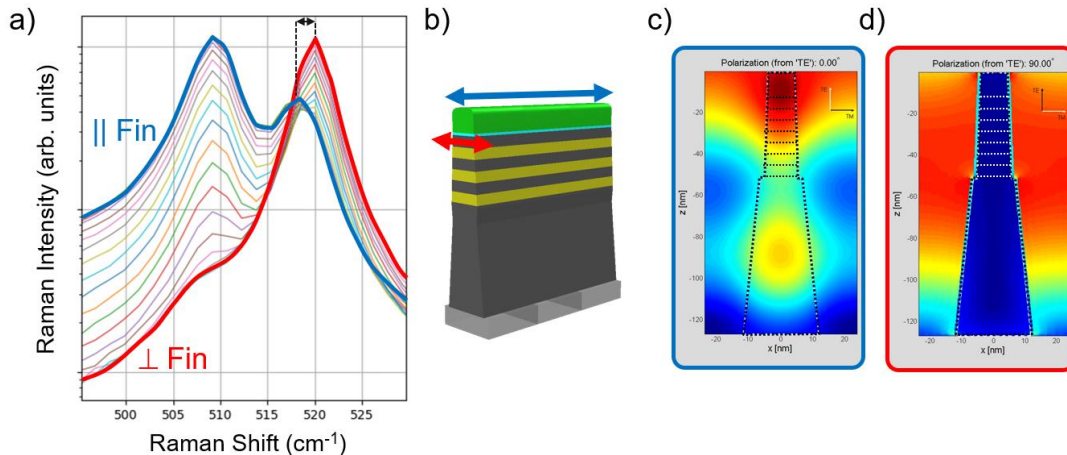


Figure 1. (a) Raman scattering intensity as a function of wavenumber and polarization orientation for a patterned stack of alternating SiGe<sub>35</sub> and Si layers on a Si substrate. The polarization direction is gradually rotated from parallel (blue) to perpendicular (red) to the fins; (b) schematic of the fin with the multilayer nanosheet stack, the arrows indicate parallel (blue) and perpendicular (red) configurations; FDTD simulations for (c) parallel and (d) perpendicular polarizations illustrate the electric field distribution.

Figure 2 depicts Raman spectra acquired before patterning for the three sample scenarios with varying Ge content that are considered for this study (SiGe<sub>25</sub>, SiGe<sub>35</sub>, SiGe<sub>50</sub>). Additionally, a representative high-angle annular dark-field (HAADF) STEM cross-section image and qualitative elemental maps of Si and Ge for the SiGe<sub>35</sub> sample post fin patterning are presented. The Raman spectra are dominated by optic phonons involving Ge-Ge, Si-Ge, and Si-Si stretching motions at around 300, 400, and 500 cm<sup>-1</sup>, respectively. In addition to these peaks, each spectrum contains some more weak features between 425 and 475 cm<sup>-1</sup>. Careful examination of the spectra shows that the Ge-Ge and the Si-Ge vibrational modes are shifting to higher wavenumbers when the alloy becomes more germanium-rich. The Si-Si stretching mode is split and two peaks appear: one at around 520 cm<sup>-1</sup> independent of the Ge content and another one below that shifts to lower wavenumbers with increasing Ge content. This behavior is well understood, and several studies have investigated and characterized the mode shifts.<sup>15,16</sup> The most intense Raman peak at around 520 cm<sup>-1</sup> originates from Si-Si optic phonons in the strain free Si substrate. The second, smaller peak adjacent to it is caused by Si-Si stretching motions within Si<sub>(1-x)</sub>Ge<sub>x</sub> layers and therefore depends on the Ge content  $x$ .

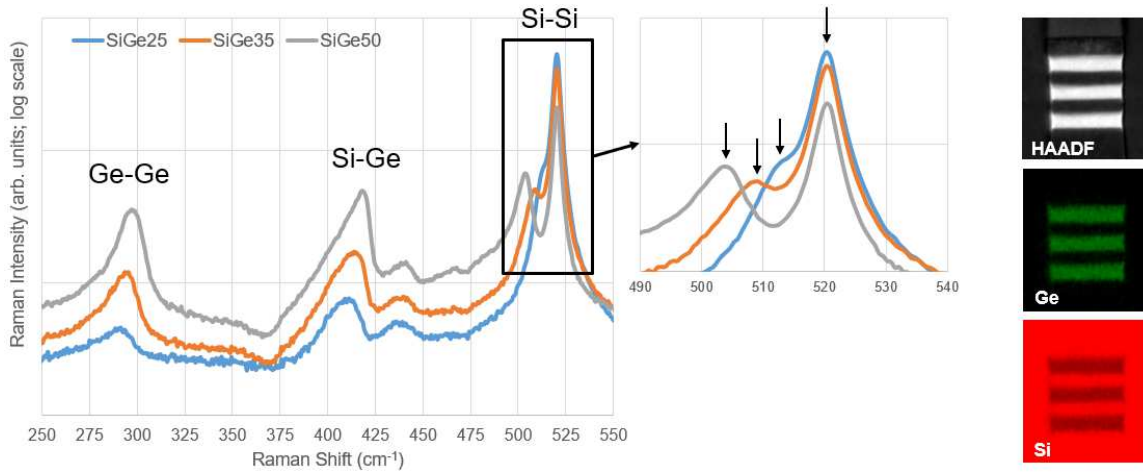


Figure 2. Raman spectra of the three nanosheet stack samples under investigation (SiGe<sub>25</sub>, SiGe<sub>35</sub>, SiGe<sub>50</sub>) acquired after deposition and before patterning. The images on the right show a representative dark-field cross-section of the SiGe<sub>35</sub> after the first patterning step (top) together with qualitative elemental mapping of Ge (middle) and Si (bottom).

In addition to composition, the three optic phonon modes Si-Si, Si-Ge, and Ge-Ge also exhibit a characteristic shift in the presence of external strain  $\epsilon$ . For this study, composition  $x$  and strain  $\epsilon$  of all samples are calculated based on expressions for the experimentally determined peak positions of Si-Si ( $\omega_{Si-Si}$ ) and Si-Ge ( $\omega_{Si-Ge}$ ) published by Tsang *et al.*<sup>15</sup>:

$$\omega_{Si-Si} = 520.2 - 62.0x - 815\epsilon, \quad (1)$$

$$\omega_{Si-Ge} = 400.5 + 14.2x - 576\epsilon. \quad (2)$$

These empirical linear approximations are very good descriptions for samples with a Ge content of  $0 < x < 0.5$ . The Ge-Ge mode, the weakest of all three, it is not considered for any compositional or strain calculations here. As observed in Figure 2, and confirmed by Eqs. (1) and (2), the Si-Si and Si-Ge phonon mode shift to lower and higher wavenumbers with increasing Ge content  $x$ , respectively. In the case of external strain, both modes red-shift to lower wavenumbers but with different slopes.

## 4. RESULTS AND DISCUSSION

### 4.1 Comparison to Reference Metrology

To evaluate the validity of composition and strain results obtained by Raman scattering peak analyses and subsequent calculations with Eqs. (1) and (2) the data can be compared to reference metrology. First, the crystal quality of all wafers is evaluated by RSMs acquired in the vicinity of the asymmetric (113) Bragg reflection (Figure 3a-c). The maps confirm

that all samples are fully strained as evidenced by the fact that the diffraction peaks from the substrate and the  $\text{Si}_{(1-x)}\text{Ge}_x$  layers line up in the horizontal direction. Furthermore, the absence of any dislocation scatter around the diffraction peaks from the layers indicates a defect-free pseudomorphic growth.<sup>12</sup>

The sheet-specific Ge content of each wafer is determined by fitting the acquired  $\omega$ - $2\theta$  XRD scans around the (004) Bragg reflection. The average Ge content of all three SiGe sheets is then compared to Raman, which also measures an average of the probed sheets, from the same five locations. The correlation plot of XRD and Raman results for composition shows that both techniques are in excellent agreement with  $R^2 = 0.996$  and a slope close to one (Figure 3d). Furthermore, the actual Ge content is close to target. Figure 3e depicts the correlation plot of the in-plane strain as determined by Raman and XRD. Equally good agreements are observed as for composition. Note that the XRD strain values are calculated, location-specific averages of all three  $\text{Si}_{(1-x)}\text{Ge}_x$  sheets using the XRD determined Ge content and assuming fully strained layers. Raman results yield a compressive strain of about -0.9% for wafers with  $x = 0.25$  and -1.8% for wafers with  $x = 0.5$ . It is noticeable, that the agreement between both techniques for the wafer with the nominally  $\text{SiGe}_{50}$  layers is not as good as for the other two wafers with  $\text{SiGe}_{25}$  and  $\text{SiGe}_{35}$  sheets. This is attributed to the fact that  $x = 0.5$  is just beyond the validity range of Eq. (2). Specifically, for germanium-rich alloys, the linear approximation used here starts failing to describe the Ge content dependent Raman shift behavior of the Si-Ge phonon accurately.<sup>17</sup> Hence, with equations optimized for germanium-rich alloys an accuracy improvement between Raman and XRD can be expected.

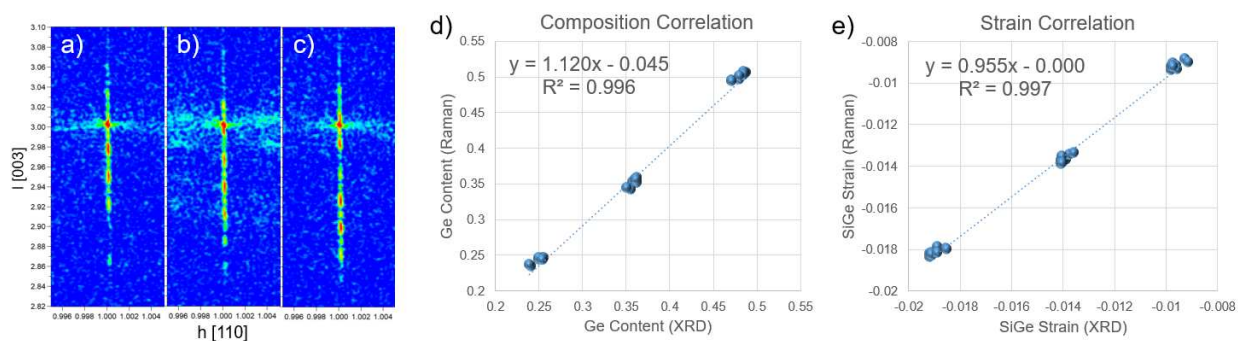


Figure 3. Measured RSMs in the vicinity of the asymmetric (113) reflection from fully strained nanosheet stacks with (a)  $\text{SiGe}_{25}$ , (b)  $\text{SiGe}_{35}$ , and (c)  $\text{SiGe}_{50}$  layers; and correlation plots for results from Raman spectroscopy and XRD for (d) composition and (e) strain.

Another comparison to reference was done after fin patterning, i.e. after the nanosheet stack is etched to form a line and space grating-like structure. Here, the reference technique is destructive PED and fins with a CD of 50 nm were characterized. Figure 4 shows cross-fin HAADF STEM images of all three samples together with the corresponding in-plane PED lattice deformation maps. The color coding refers to the lattice parameter change relative to the unstrained Si substrate. It is evident that the patterning leads to a partial relaxation within the  $\text{Si}_{(1-x)}\text{Ge}_x$  sheets, which is most pronounced at the edges and due to the creation of the unconstrained surfaces. The in-plane deformation and calculated relaxation are proportional to the Ge content and most pronounced for the wafer with  $\text{SiGe}_{50}$  sheets. The average relaxation along the  $x$ -direction considering the lattice deformation of all three sheets is 40.4%, 71.8%, and 75.0% for the wafers with  $\text{SiGe}_{25}$ ,  $\text{SiGe}_{35}$ , and  $\text{SiGe}_{50}$  sheets, respectively.

Furthermore, relaxation of the compressively strained  $\text{Si}_{(1-x)}\text{Ge}_x$  sheets induces a tensile strain within the Si sheets. The finite element method (FEM) simulation depicted for the sample with the  $\text{SiGe}_{35}$  sheets is in good agreement with the PED maps and illustrates the above discussed behaviors clearly.<sup>5,6</sup> For this study, no PED lattice deformation maps along the fins were obtained (along the  $y$ -direction). However, it is known from previous studies on wafers manufactured in an identical fashion that, for practically infinitely long fins, no relaxation occurs and the SiGe sheets are still fully strained.<sup>7</sup> Simulations for fins with a length of 500 nm show that due to the Poisson effect tensile strain also appears in the Si sheets along the fins ( $y$ -direction), although at lower amounts.<sup>5</sup> The  $y$ -direction becomes the channel and hence transport direction, and therefore the induced strain is beneficial for nFET devices since electron mobility is increased in tensile Si.

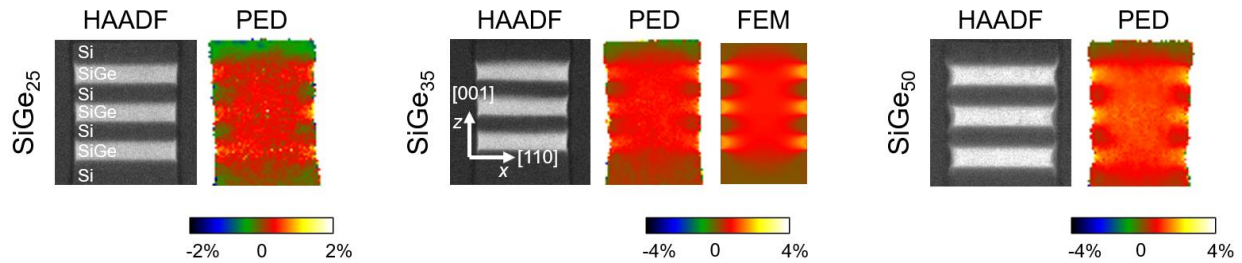


Figure 4. HAADF STEM and corresponding PED lattice deformation maps for SiGe<sub>25</sub>, SiGe<sub>35</sub>, and SiGe<sub>50</sub>. The scale bar denotes the lattice deformation with respect to the unstrained Si substrate. The FEM simulation for the SiGe<sub>35</sub> sample is also shown for clarity.

To compare the PED strain results with Raman, first the average in-plane strain was calculated by averaging the sampled values across fin with the value for the respective fully strained direction along the fin. The computed average PED in-plane strain is then compared with the strain from Raman using scattering results obtained with polarization perpendicular to the fin direction and the correlation is depicted in Figure 5. Both results are in good agreement with  $R^2 = 0.93$  and a slope of greater than 0.9.

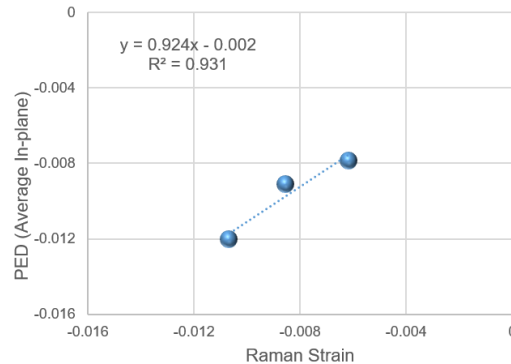


Figure 5. Average in-plane strain obtained by PED in comparison with Raman results obtained with polarization perpendicular to the fin direction.

## 4.2 Raman Strain Monitoring

With the assurance that strain results obtained by Raman spectroscopy are in good agreement with reference metrology for blanket and patterned targets, all presented strain results from here on are from Raman metrology only. Figure 6a illustrates the compressive strain in Si<sub>(1-x)</sub>Ge<sub>x</sub> sheets for all three samples as a function of all 21 dies measured across the wafer. The four graphs correspond to measurements of an unpatterned blanket target and three patterned targets with different fin CDs (40, 50, and 70 nm). A representative cross-section of the patterned target with 40 nm fin CD is also depicted (inset in Figure 6b). As discussed already before, the strain increases with Ge content due to the increasing lattice mismatch. The consistent measurements across the wafer indicate that metrology noise and processing variations are very low, and no across wafer signature is observed. The average across wafer Ge content determined by Raman is 25.2, 37.2, and 49.2% for the nominally SiGe<sub>25</sub>, SiGe<sub>35</sub>, and SiGe<sub>50</sub> samples, respectively. With patterning and the creation of unconstrained surfaces, relaxation occurs, which depends on the fin CD, i.e., with smaller CDs greater relaxation is observed. This can be explained with the increasing surface to volume ratio with decreasing CDs and hence the increasing dominance of the strong edge relaxation. Across the three samples, the average relaxation is approximately constant with 19, 22, and 25% for the 70, 50, and 40 nm features, respectively.

Figure 6b shows the same graph but for tensile Si sheets. Note that at the unpatterned blanket stage, the Si sheets do not exhibit any strain. In this case, the Si-Si LO-TO Raman phonon of the unstrained Si sheets is identical to the phonon mode of the strain-free Si substrate. Hence the simulated data points at zero strain are not measurements and only added for

convenience. Once the blanket multilayer stack is patterned and the strained  $\text{Si}_{(1-x)}\text{Ge}_x$  relaxes, a tensile strain is induced in the Si sheets. The tensile strain in Si depends on the Ge content within the  $\text{Si}_{(1-x)}\text{Ge}_x$  and on the sheet CD. The Si strain for the wafer with the  $\text{SiGe}_{50}$  sheets is about a factor of two larger compared to the stacks with  $\text{SiGe}_{25}$  sheets. Furthermore, the sheets with the smallest CD (40 nm) exhibit the largest strain and there is an approximately linear relationship between strain and CD within the measured range.

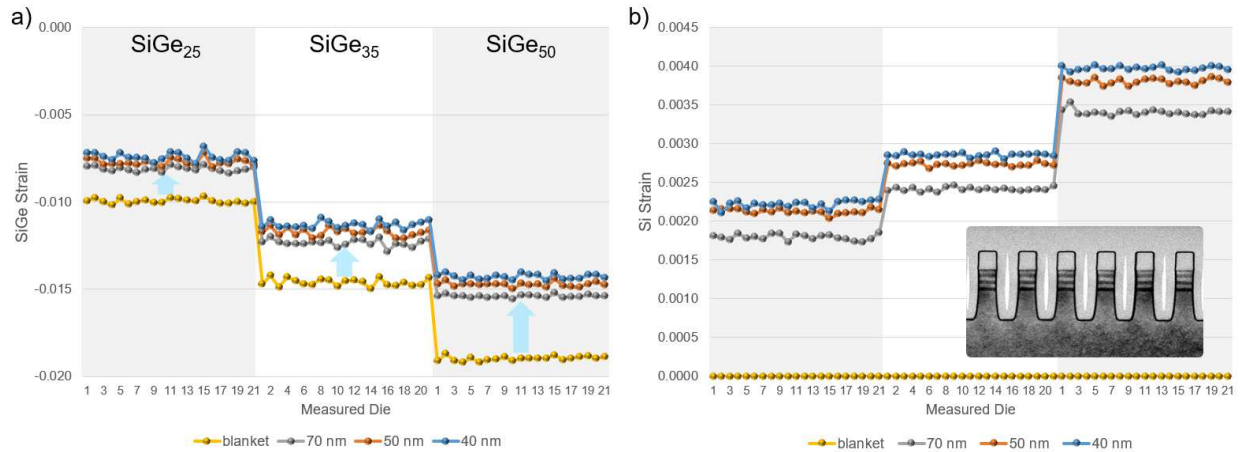


Figure 6.  $\text{Si}_{(1-x)}\text{Ge}_x$  (a) and Si (b) strain for blanket and three different fin CDs (40, 50, and 70 nm) as a function of measured dies across the wafer. The three vertical sections in (a) and (b) represent the three different samples with  $\text{SiGe}_{25}$ ,  $\text{SiGe}_{35}$ ,  $\text{SiGe}_{50}$  sheets. The inset in (b) shows a STEM cross-section of the  $\text{SiGe}_{25}$  sample with 40 nm fin CD. All results are obtained with polarization along the fin direction.

As discussed earlier already, measured strain also depends on the polarization direction of the probing light. Polarization-dependent results of the compressive strain in  $\text{Si}_{(1-x)}\text{Ge}_x$  after fin patterning are shown in Figure 7. The box chart is vertically sectioned accommodating the three sample scenarios and the  $x$ -axis sorts the four targets by increasing CD (the unpatterned blanket can be understood as having an infinitely large CD). The blanket strain probed with parallel and perpendicular polarization states is practically identical. This is expected as the Raman peak position for two orthogonal directions from a Si (100) wafer are identical.<sup>14</sup> The patterned sites on the other hand exhibit a strong polarization-dependent strain difference. When probing the strain with polarization parallel to the fins, the value is larger compared to a polarization perpendicular to the fins. This general observation is also in agreement with previously published PED results and corresponding simulations.<sup>5</sup> Furthermore, the compressive strain difference increases significantly with decreasing CD, and the measurement with perpendicular polarization is more sensitive to CD changes. In general, the trend for the wafers with different Ge concentrations are comparable but differ in amplitude. Note that the far-field Raman scattering of patterned Si and  $\text{Si}_{(1-x)}\text{Ge}_x$  nanosheet stacks is a complex response depending on electric field localizations, polarization dependent selection rules for backscattering from the (001) surface (relaxed due to patterning), and three different phonon modes.<sup>11,18</sup> Simulations show that with a polarization along the fin direction the electric field is mostly localized within the fin with a dominant LO phonon (Figure 1c). In this measurement configuration the strain in the center of the fin along the fully strained direction is the dominant part of the signal. In the orthogonal direction, while the electric field is mostly excluded from the fins (Figure 1d), the three phonon modes ( $\text{TO}_1$ ,  $\text{TO}_2$ , and LO) related to the nanosheet stack contribute similarly to Raman scattering from all parts of the sheets. This happens to be a very good measure of the average in-plane strain here as shown in Figure 5. Detailed in-plane strain decomposition is possible by analyzing multiple polarization-dependent metrology configurations but is beyond the scope of this work.

### 4.3 Strain Tracking Through FEOL Patterning

Figure 8 shows the  $\text{SiGe}_{25}$  strain evolution through FEOL patterning after six important processing steps: blanket (nanosheet stack deposition), FinRIE (fin patterning along  $y$ ; “nanosheet stack lines”), GateRIE (dummy gate patterning), FinRecess (fin patterning along  $x$ ; “nanosheet stack pillars”), S/D epi (Si:P epitaxy), and PolyPull (dummy gate removal).

The five insets at the top schematically depict the structure at the respective processing step with an orientation parallel to the original fin direction (channel direction). PolyPull is the last opportunity to measure the sacrificial  $\text{Si}_{(1-x)}\text{Ge}_x$  sheets as they get removed at the next processing step. Focus is put on nFET devices and polarization along the y-direction (original fin direction). The boxes and whiskers represent measured values for all fin and gate CDs and indicate the across wafer variation convoluted with some metrology uncertainty.

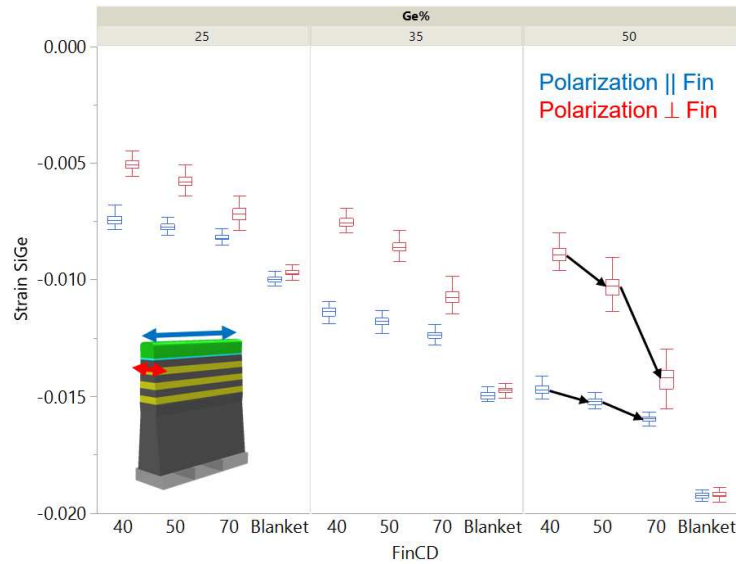


Figure 7. Polarization dependence of  $\text{Si}_{(1-x)}\text{Ge}_x$  strain results post fin RIE. The chart is split into three vertical sections representing the three sample types with different Ge content under investigation. The x-axis within each section groups the results by fin CD and includes the unpatterned blanket site. The blue and red boxes denote the results for polarization parallel and perpendicular to the fins, respectively. The black arrows are merely a guide to the eye.

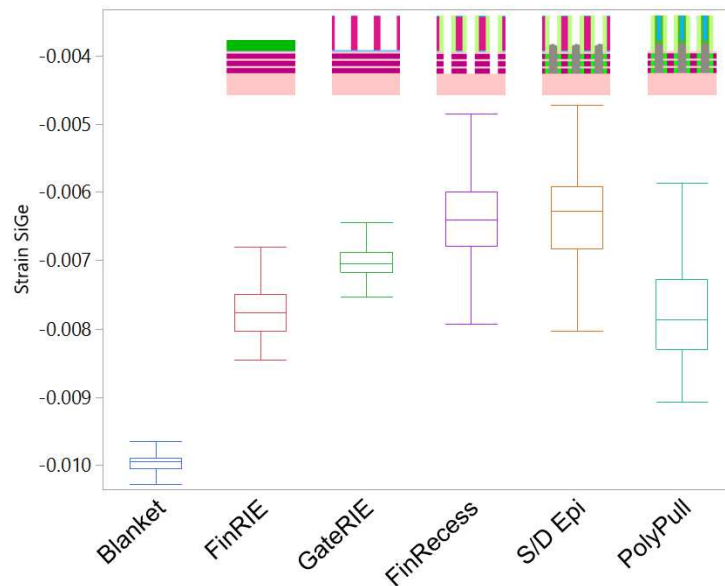


Figure 8.  $\text{SiGe}_{25}$  strain evolution through FEOL patterning measured after six processing steps. Results depicted are for nFET devices and polarization along the y-direction. The insets at the top schematically depict the structure at the respective processing step with a view parallel to the y-direction (along the fins).

As discussed before, processing starts with fully strained SiGe<sub>25</sub> layers at the blanket stage due to a defect-free pseudomorphic growth. After the first patterning step (FinRIE) already the most significant impact on strain is observed with on average >20% relaxation. At GateRIE a small relaxation is observed, which is mostly attributed to several thermal processing steps within the fin module. Note that at GateRIE the major contribution to the Raman response is from the exposed fin areas not covered by the dummy gate. The next step is FinRecess, which is a fin patterning perpendicular to the original fin direction defining the gate length. This leaves nanosheet stack pillars with dimensions of the fin CD in one direction and dummy gate CD in the other direction. On average, some further relaxation is observed, which is due to the creation of more unconstrained surfaces. Additionally, an increase in the data spread is noticed and mainly caused by the influence of the now present and varying gate CD. Similar to previously discussed trends related to the fin CD, with decreasing gate CD the sheet relaxation increases but not as dramatic as compared to what was measured at FinRIE. Nonetheless, the gate CD-dependent strain behavior does not explain all observed variation. The reduced amount of sheet volume together with the polycrystalline dummy gate, which causes a broad Raman background thereby contributing to measurement uncertainty, and likely some process related variations add to the overall data spread. Note that light needs to pass through the polycrystalline dummy gate twice before Raman scattering can be collected.

For this wafer, the strain remains approximately constant after S/D epitaxy with an equally large distribution. After PolyPull, when all polycrystalline dummy gate material is removed, an increased compressive SiGe<sub>25</sub> strain is measured again. Further studies also supported by strain modeling are required to fully understand what is happening. Possibilities may be related to dummy gate clamping, S/D epi strain, processing, or strain modeling inaccuracies due to the polycrystalline material at the previous steps.

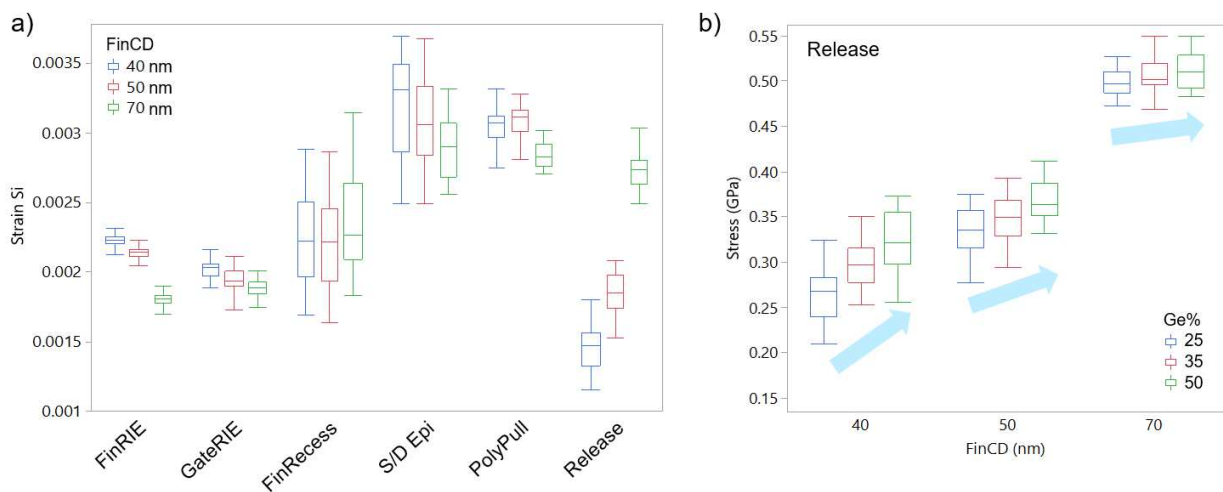


Figure 9. (a) Tensile Si strain evolution through FEOL patterning measured after six processing steps, where each box per step represents a different fin CD. Results depicted are for nFET devices with SiGe<sub>25</sub> sheets; (b) Si stress post channel release as a function of fin CD and Ge%. Only strain and stress values from measurements with polarization along the y-direction are compared.

Figure 9a depicts the Si tensile strain evolution through FEOL patterning after six important processing steps: FinRIE, GateRIE, FinRecess, S/D epi, PolyPull, and Release. The latter step refers to the removal of the sacrificial SiGe<sub>25</sub> sheets. At each step the strain is plotted for all three fin CDs. The boxes and whiskers represent all measured values and the across wafer variation convoluted with some metrology uncertainty. Note that the blanket step is not included because the Si sheets do not exhibit any strain before patterning. The results at FinRIE have been discussed in detail already above (Figure 6b); briefly, CD-dependent tensile strain is generated by the SiGe<sub>25</sub> relaxation. It is noticeable at GateRIE that the difference between the three fin CDs is less pronounced as compared to FinRIE and mainly related to the strain decrease of the 40 and 50 nm device structures. This may be caused by thermal processing in the fin module. At FinRecess, there is a small increase in strain due to further edge relaxation of the SiGe<sub>25</sub> sheets along with a significant increase in the data spread. This data spread increase was also observed for the SiGe<sub>25</sub> strain at the same process step and is related to the different gate CDs with additional contributions from possible process variations and an increased measurement

uncertainty due to the smaller Si sheet area located underneath the thick polycrystalline gates. A substantial increase post S/D epitaxy is observed with no major strain changes transitioning to PolyPull. After removal of the polycrystalline dummy gate material the data spread decreases again slightly. Note that since the measured devices are nFETs, the S/D and the channel are comprised of epitaxial Si. It has been confirmed that the selected experimental settings allow for probing the Si nanosheet channels only, independent of the S/D region. Choosing a different measurement configuration, it is possible to probe the S/D epitaxial Si:P only.

After the complete removal of the sacrificial SiGe<sub>25</sub> nanosheets (Release), a significant size-dependent strain relaxation is observed. However, the Si nanosheets still remain under tensile strain. Now, the smallest fin CD exhibits also the smallest tensile strain and with increasing CD the strain increases substantially. This trend is opposite to what was observed at FinRIE and likely related to edge relaxation, which is more pronounced when the surface to volume ratio is large. The gate CD plays a minor role only at PolyPull and Release and is not discussed.

A more detailed analysis after the Release step is presented in Figure 9b. The Si strain was converted to stress in GPa using a Young's modulus  $E = 180$  GPa. Besides looking at CD-dependent stress behavior, results from the wafers with different Ge content are presented. For each measured CD, the stress increases with Ge content. This means that strain tuning of the Si channel is possible by variation of the Ge content in the sacrificial Si<sub>(1-x)</sub>Ge<sub>x</sub> nanosheets.

Most observed trends are in agreement with previously published simulations by Reboh *et al.*<sup>6</sup> Specifically, the emergence of tensile strain after fin patterning and the fact that tensile strain post channel release depends on the Ge content of the sacrificial Si<sub>(1-x)</sub>Ge<sub>x</sub> nanosheets. Notably, simulations suggest an average stress of approximately 0.3 GPa for devices using sacrificial SiGe<sub>30</sub>, which is close to what is measured by Raman spectroscopy on wafer.

## 5. CONCLUSIONS AND OUTLOOK

In-line Raman spectroscopy for Si and Si<sub>(1-x)</sub>Ge<sub>x</sub> nanosheet strain metrology throughout the front-end-of-line manufacturing cycle of next-generation stacked gate-all-around nanosheet field-effect transistors was presented and results discussed. Three samples with intentional strain variations, by changing the Ge content ( $x = 0.25, 0.35, 0.50$ ) of the pseudomorphic Si<sub>(1-x)</sub>Ge<sub>x</sub> nanosheets, were manufactured and measured at seven critical processing steps using polarization-dependent in-line Raman spectroscopy. To characterize and quantify the strain evolution, the precise position of the Si-Si and Si-Ge optical phonon modes was determined at each process step, based on which composition and strain can be calculated.

The importance of excitation wavelength was discussed with regards to penetration depths and scattering cross-sections. It was highlighted how critical polarization-dependent measurements are for blanket films and particularly when evaluating patterned anisotropic samples. Especially when characterizing orientation-dependent strain or when epitaxial Si in channel and source/drain needs to be characterized independently, for instance. While a detailed strain decomposition was not within the scope of this work, it was demonstrated that excitations parallel and perpendicular to patterned fins yield different strain results and the observed trends agree with PED and simulations.<sup>5</sup>

The accuracy of the Raman metrology was confirmed with reference data for composition and strain obtained after nanosheet stack epitaxy on unpatterned targets by non-destructive high-resolution x-ray diffraction. It was found that both methodologies are in excellent agreement. Additionally, lattice deformation maps determined from precession electron diffraction after the first line and space patterning were used to calculate strain. A comparison to Raman spectroscopy revealed a very good agreement and helped understanding of polarization-dependent settings.

Monitoring the strain evolution of Si sheets through patterning processes, it was found that the experimentally determined results from in-line Raman spectroscopy follow trends of previously published simulations.<sup>6</sup> Specifically, a successively increasing relaxation of the compressive Si<sub>(1-x)</sub>Ge<sub>x</sub> strain after FinRIE (nanosheet stack lines) and FinRecess (nanosheet stack pillars) induces an increasing tensile strain in the Si sheets. The strain is strongly size-dependent, and the tensile Si sheet strain can be engineered by Ge content variation of the sacrificial layers. The absolute value of the calculated Si nanosheet stress post channel release agrees with FEM simulations.

The presented in-line Raman metrology is developed for non-destructive nFET device baseline monitoring. Even more important is strain metrology for pFET devices particularly because complex strain engineering approaches are developed to boost hole mobility.<sup>4</sup> While the electron mobility in nanosheet devices is much better compared to finFETs due to the

channel orientation and the intrinsic tensile strain induced by the sacrificial sheets, the hole mobility in the same channels is rather low. Therefore, compressive  $\text{Si}_{(1-x)}\text{Ge}_x$  channels are desired. Front-up dual processing is complex and costly, hence an ‘SiGe channel last’ approach has been proposed recently.<sup>4</sup> The innovative part starts post  $\text{Si}_{(1-x)}\text{Ge}_x$  channel release and the method relies on trimming down the Si channels to a thickness of about 2 nm before growing a pseudomorphic  $\text{Si}_{(1-x)}\text{Ge}_x$  cladding all around the channel. In-line strain monitoring with Raman spectroscopy at multiple processing steps within this flow (e.g. after trimming and after  $\text{Si}_{(1-x)}\text{Ge}_x$  growth) will be an invaluable addition to ensure successful development and consistent high volume manufacturing of these next-generation gate-all-around nanosheet devices.

## 6. ACKNOWLEDGEMENTS

The authors would like to thank Marjorie Cheng, Jennifer Fullam, Gilad Barak, John Gaudiello, Raja Muthinti, Michael Sandler, Mary Breton, Nelson Felix, and Bala Haran for support of this work.

## REFERENCES

- [1] M. Lapedus, “New Transistor Structures At 3nm/2nm,” 25 January 2021, <<https://semiengineering.com/new-transistor-structures-at-3nm-2nm/>> (02 February 2021)
- [2] N. Loubet, T. Hook, P. Montanini, C.-W. Yeung, S. Kanakasabapathy, M. Guillom, T. Yamashita, J. Zhang, X. Miao, J. Wang, A. Young, R. Chao, M. Kang, Z. Liu, S. Fan, B. Hamieh, S. Sieg, Y. Mignot, W. Xu, S.-C. Seo, J. Yoo, S. Mochizuki, M. Sankarapandian, O. Kwon, A. Carr, A. Greene, Y. Park, J. Frougier, R. Galatage, R. Bao, J. Shearer, R. Conti, H. Song, D. Lee, D. Kong, Y. Xu, A. Arceo, Z. Bi, P. Xu, R. Muthinti, J. Li, R. Wong, D. Brown, P. Oldiges, R. Robison, J. Arnold, N. Felix, S. Skordas, J. Gaudiello, T. Standaert, H. Jagannathan, D. Corliss, M.-H. Na, A. Knorr, T. Wu, D. Gupta, S. Lian, R. Divakaruni, T. Gow, C. Labelle, S. Lee, V. Paruchuri, H. Bu, M. Khare, “Stacked Nanosheet Gate-All-Around Transistor to Enable Scaling Beyond FinFET,” *Symp. VLSI Tech.*, 230–231 (2017).
- [3] G. Tsutsui, S. Mochizuki, N. Loubet, S. W. Bedell, D. K. Sadana, “Strain engineering in functional materials,” *AIP Advances* 9, 030701 (2019).
- [4] S. Mochizuki, M. Bhuiyan, J. Zhang, H. Zhou, E. Stuckert, J. Li, K. Zhao, M. Wang, V. Basker, N. Loubet, D. Guo, B. Haran, H. Bu, “Stacked Gate-All-Around Nanosheet PFET with Highly Compressive Strained SiGe Channel,” 2020 IEEE International Electron Devices Meeting (IEDM).
- [5] S. Reboh, R. Coquand, N. Loubet, N. Bernier, E. Augendre, R. Chao, J. Li, J. Zhang, R. Muthinti, V. Boureau, T. Yamashita, O. Faynot, “Imaging, Modeling and Engineering of Strain in Gate-All-Around Nanosheet Transistors,” 2019 IEEE International Electron Devices Meeting (IEDM).
- [6] S. Reboh, R. Coquand, S. Barraud, N. Loubet, N. Bernier, G. Audoit, J.-L. Rouviere, E. Augendre, J. Li, J. Gaudiello, N. Gambacorti, T. Yamashita, O. Faynot “Strain, stress, and mechanical relaxation in fin-patterned Si/SiGe multilayers for sub-7 nm nanosheet gate-all-around device technology”, *Appl. Phys. Lett.* 112, 051901 (2018).
- [7] J. Li, S. Mochizuki, J. Zhang, N. Loubet, J. Gaudiello, B. Haran, “Precession Electron Diffraction (PED) Strain Measurements in Stacked Nanosheet Structures,” *Microsc. Microanal.* 25, Suppl 2 (2019).
- [8] A. Schulze, R. Loo, L. Witters, H. Mertens, A. Gawlik, N. Horiguchi, N. Collaert, M. Wormington, P. Ryan, W. Vandervorst, M. Caymax, “Strain and Compositional Analysis of (Si)Ge Fin Structures Using High Resolution X-Ray Diffraction,” *Phys. Status Solidi C* 14, 1700156 (2017).
- [9] D. De Salvador, M. Petrovich, M. Berti, F. Romanato, E. Napolitani, A. Drigo, J. Stangl, S. Zerlauth, M. Mühlberger, F. Schäffler, G. Bauer, P.C. Kelires, “Lattice parameter of  $\text{Si}_{1-x-y}\text{Ge}_x\text{C}_y$  alloys,” *Phys. Rev. B* 61, 12005 (2000).
- [10] I. De Wolf, “Micro-Raman spectroscopy to study local mechanical stress in silicon integrated circuits,” *Semicond. Sci. Technol.* 11, 139 (1996).
- [11] T. Nuytten, T. Hantschel, D. Kosemura, A. Schulze, I. De Wolf, W. Vandervorst, “Edge-enhanced Raman scattering in narrow Ge fin field-effect transistor channels,” *Appl. Phys. Lett.* 106, 033107 (2015).
- [12] M. Kuhn, S. Cea, J. Zhang, M. Wormington, T. Nuytten, I. De Wolf, J.-M. Zuo, J.-L. Rouviere, in *Metrology and Diagnostic Techniques for Nanoelectronics*, edited by Z. Ma and D.G. Seiler (Pan Stanford, Singapore, 2017).

- [13] A. Picco, E. Bonera, E. Grilli, M. Guzzi, M. Giarola, G. Mariotto, D. Chrastina, G. Isella, "Raman efficiency in SiGe alloys," *Phys. Rev. B* 82, 115317 (2010).
- [14] W.S. Yoo, H. Harima, M. Yoshimoto, "Polarized Raman Signals from Si Wafers: Dependence of In-Plane Incident Orientation of Probing Light," *ECS J. Solid State Sc.* 4, P356 (2015).
- [15] J.C. Tsang, P.M. Mooney, F. Dacol, J.O. Chu, "Measurements of alloy composition and strain in thin  $\text{Ge}_x\text{Si}_{1-x}$  layers," *J. Appl. Phys.* 75, 8098 (1994).
- [16] H. Rucker, M. Methfessel, "Anharmonic Keating model for group-IV semiconductors with application to the lattice dynamics in alloys of Si, Ge, and C," *Phys. Rev. B* 52, 11059 (1995).
- [17] M.I. Alonso, K. Winer, "Raman spectra of  $c\text{-Si}_{1-x}\text{Ge}_x$  alloys," *Phys. Rev. B* 39, 10056 (1989).
- [18] V. Poborchii, T. Tada, T. Kanayama, "Edge-enhanced Raman scattering in Si nanostripes," *Appl. Phys. Lett.* 94, 131907 (2009).